Available online at www.sciencedirect.com
SCIENCE DIRECT®
Acta Materialia 53 (2005) 4259–4268
Acta MATERIALIA
www.actamat-journals.com

Coarsening kinetics of nanoscale Al_3Sc precipitates in an Al–Mg–Sc alloy

Emmanuelle A. Marquis [a,b], David N. Seidman [b,*]

[a] *Materials Physics Department, Sandia National Laboratories, Livermore, CA 94550, United States*
[b] *Materials Science and Engineering Department, Northwestern University, Evanston, IL 60208-3108, United States*

Received 30 March 2005; received in revised form 16 May 2005; accepted 18 May 2005
Available online 12 July 2005

Abstract

The effects of Mg alloying on the temporal evolution of Al_3Sc ($L1_2$ structure) nanoscale precipitates are investigated, focusing on the morphology and coarsening kinetics of Al_3Sc precipitates in an Al–2.2 Mg–0.12 Sc at.% alloy aged between 300 and 400 °C. Approximately spheroidal precipitates are obtained after aging at 300 °C and irregular morphologies are observed at 400 °C. The coarsening behavior is studied using conventional and high-resolution transmission electron microscopies to obtain the temporal evolution of the precipitate radius, and atom-probe tomography is employed to measure the Sc concentration in the α-matrix. The coarsening kinetics are analyzed using a coarsening model developed by Kuehmann and Voorhees for ternary systems [Kuehmann CJ, Voorhees PW. Metall Mater Trans A 1996;27:937]. Values of the interfacial free energy and diffusion coefficient for Sc diffusion in this Al–Mg–Sc alloy at 300 °C are independently calculated, and are in good agreement with the calculated value of interfacial free energy [Asta M, Ozolins V, Woodward C. JOM 2001;53:16] and the experimental diffusivity obtained for the Al–Sc system [Marquis EA, Seidman DN. Acta Mater 2001;49:1909; Marquis EA. Ph.D. Thesis. Materials Science and Engineering Department, Northwestern University, 2002; Fujikawa SI. Defect Diffusion Forum 1997;143–147:115].

Keywords: Al_3Sc precipitate; Morphology; Coarsening; Transmission electron microscopy; Atom-probe tomography

1. Introduction

Aluminum alloys containing Sc are promising materials for high-temperature structural applications due to the high strengthening effect of the Al_3Sc ($L1_2$) precipitates [6,7]. Strengthening improvements and nanostructural stability of Al–Sc base alloys are achieved by adding alloying elements, such as Zr, thereby decreasing the coarsening kinetics of the precipitates [6], and Mg as a solid-solution strengthener [6]. It is important to understand the effects of Mg in order to control not only the specific contribution of Mg to the properties of Al–Sc alloys (strengthening effect and creep resistance) but also the changes in the nanostructure.

The combined Mg and Sc solid-solubilities in Al are reduced compared to the respective binary Al–Mg and Al–Sc systems. The Al-rich corner of the pseudo-binary Al–2.2 at.% Mg–Sc phase diagram, calculated by Murray (from Alcoa) [8], is shown in Fig. 1; note well that this isopleth exhibits a very narrow solid-solubility range of Sc in Al containing 2.2 at.% Mg, that is, 7.2×10^{-4} at.% Sc at 300 °C. Pisch et al. [9] measured even smaller Sc solid-solubility values, 8×10^{-5} at.% Sc at 300 °C for 2.2 at.% Mg. The solubility of Mg in the Al_3Sc phase is still not clearly determined. First principles calculations, however, predict the absence of Mg in the Al_3Sc phase [2]. Magnesium was, however, found at up to 5 at.% in the Al_3Sc phase after annealing at 350 °C for 60 days

* Corresponding author. Tel.: +1 847 491 4391.
E-mail address: d-seidman@northwestern.edu (D.N. Seidman).

1359-6454/$30.00
doi:10.1016/j.actamat.2005.05.025

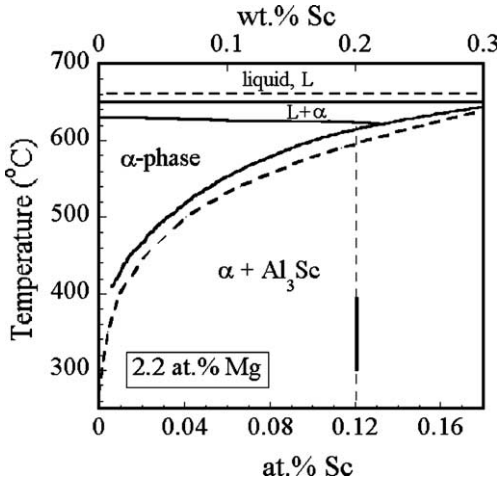

Fig. 1. Al-rich corner of the Al–2.2 at.% Mg–Sc phase diagram as calculated by Murray [8]. The dashed lines represent the Al–Sc phase diagram [29]. The vertical line indicates the alloy studied in this research.

[10]. Murray calculated an equilibrium concentration of either 0 at.% Mg or 3.5 at.% Mg substituting for Sc at 300 °C for an Al–2.2 at.% Mg–0.12 at.% Sc alloy [8].

The coarsening kinetics of Al_3Sc precipitates between 300 and 450 °C in a binary Al–0.18 at.% Sc alloy are described in detail in [3,4], and they obey approximately the $(\text{time})^{1/3}$ kinetic law for the average precipitate radius, $\langle R(t)\rangle$, of the Lifshitz–Slyozov–Wagner (LSW) model for a binary alloy [11,12], yielding an activation energy for Sc diffusion in Al of 164 ± 9 kJ mol^{-1}, which is in agreement with the values obtained from tracer diffusion measurements [5]. Utilizing differential scanning calorimetry analysis, it was shown that Mg has no significant effect on the precipitation kinetics and volume fraction of Al_3Sc precipitates in an Al–4.4 Mg–0.3 Sc at.% alloy [13]. Similarly, Toporova et al. [6] studying Al alloys containing 0.24 at.% Sc and 2.77 to 7.2 at.% Mg, by microhardness measurements, concluded that the precipitation kinetics are not modified by the presence of Mg; however, no coarsening kinetics results, with precipitate radii measurements, were presented.

There are a limited number of quantitative experimental studies of the coarsening kinetics of a second phase in ternary systems [14–16]. Several workers have, however, developed models describing coarsening kinetics in multi-component systems. Umantsev and Olson [17] derived a general analytical formulation of the coarsening kinetics in multi-component systems in the absence of capillary effects, while Kuehmann and Voorhees [1] solved the problem taking into account the capillary effects for ternary alloys with low precipitate volume fractions; depending on the partitioning behavior and the diffusivities of the alloying elements, the coarsening behavior of the second phase can be strongly modified compared to the binary alloy. The effects of Mg on precipitation and the coarsening behavior of Al_3Sc precipitates in an Al–Mg–Sc alloy need to be addressed in detail, in light of these coarsening models for ternary alloys.

Building on our previous research on the precipitation behavior of Al_3Sc in dilute Al–Sc alloys, specifically focusing on precipitate morphologies and coarsening kinetics [3,4], this study focuses on the changes induced by the presence of Mg on the morphologies and the coarsening kinetics of Al_3Sc precipitates in an Al–2.2 Mg–0.12 Sc at.% alloy. Observations by conventional transmission electron (CTEM) and high resolution electron (HREM) microscopies, and atom-probe tomography (APT) analyses were performed in parallel in order to describe quantitatively the nanostructures and compositions of both α-Al matrix and Al_3Sc precipitate phases as a function of aging time and temperature. APT analyses of the behavior of Mg during Al_3Sc precipitation are discussed in separate articles [4,18]. This research is part of a comprehensive study of the room temperature and elevated temperature (573 K) creep behavior of Al(Sc) based alloys [4,19,20] in parallel with the complete characterization of their nanostructures [3,4,18].

2. Experimental procedures

An Al alloy with nominal composition 2.2 at.% Mg–0.12 at.% Sc was prepared by casting, using pure metals and a master alloy (99.9 wt.% purity Al, 99.99 purity % Mg and Al–0.35 at.% Sc), which were melted in an alumina crucible, stirred to ensure proper mixing, and directionally solidified in a graphite mold. Homogenization in the single-phase region of the ternary phase diagram (Fig. 1) was performed at 618 °C in air for 24 h to ensure uniformity of the Mg concentration throughout the alloy and eliminate the dendritic structure resulting from directional solidification. The samples were quenched into water at room temperature, and aged in air at different temperatures (300 to 400 °C) for between 0.33 and 1040 h.

Transmission electron microscopy samples were prepared by cutting the alloy into 350 μm thick foils. Discs of 3 mm diameter were punched from the foil, mechanically ground to 200 μm, and then jet electro-polished with a solution of 5 vol.% perchloric acid in methanol at −30 °C. CTEM was performed utilizing an Hitachi 8100 operating at 200 kV (Northwestern University), and HREM on a JEOL 4000EXII (Argonne National Laboratory) operating at 200 kV to limit the amount of radiation damage produced by the electron beam.

The APT tips were obtained by a two-step electropolishing procedure using a solution of 30 vol.% nitric acid in methanol followed by a solution of 2 vol.% perchloric acid in butoxyethanol. Tips were maintained at

temperatures below 30 K, with a chamber pressure of 10^{-5} torr consisting of a mixture of 80% Ne and 20% He for field-ion microscopy (FIM) observations, and ultrahigh vacuum conditions (10^{-10} torr) for pulsed field-evaporation analyses; the latter was performed using a pulse fraction (pulse voltage/steady state dc voltage) of 20% and a pulse frequency of 1500 Hz.

3. Results

3.1. Transmission electron microscopy observations

3.1.1. Precipitate morphology

After aging at 300 °C, approximately spheroidal Al_3Sc precipitates, uniformly distributed throughout the matrix, are present at a high number density. After 24 h aging, the number density is about $(4 \pm 2) \times 10^{22}$ precipitate m^{-3}, measured from CTEM micrographs (Fig. 2). The temporal evolution of the precipitate morphology projected along the [1 0 0] direction, during aging at 300 °C was observed using HREM. After 0.5 h, the small precipitates appear cuboidal (Fig. 3(a)), while after 5 h the Al_3Sc precipitates are more spheroidal (Fig. 3(b)). Longer aging times, 1040 h, lead to larger spheroidal precipitates (Fig. 3(c)). The interface between the Al_3Sc precipitates and the α-Al matrix remains coherent even for the precipitates with the larger radii ($R = 4.2$ nm), obtained after aging for 1040 h. The coherency state of the α-Al/Al_3Sc interface is ascertained by the so-called Ashby–Brown strain contrast (Fig. 2), and no interfacial misfit dislocations could be detected in the HREM micrographs, which implies the precipitates are coherent.

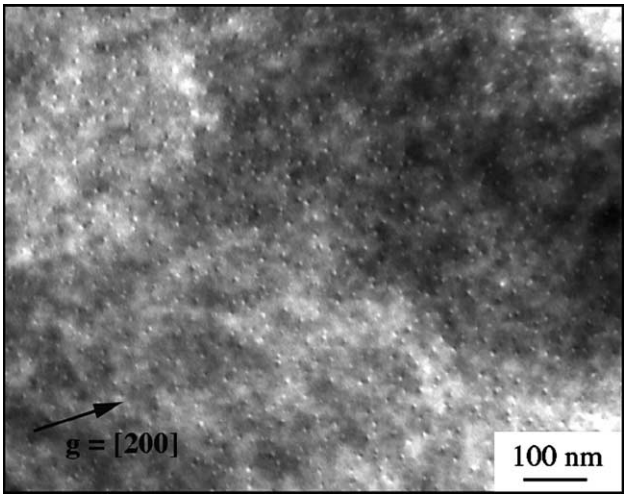

Fig. 2. CTEM micrograph showing a high number density ($4 \pm 2 \times 10^{22}$ m^{-3}) of Al_3Sc precipitates in an Al–2.2 at.% Mg–0.12 at.% Sc alloy after aging at 300 °C for 24 h: dark-field image, exhibiting Ashby–Brown strain coherency contrast, obtained with a 2 0 0 reflection.

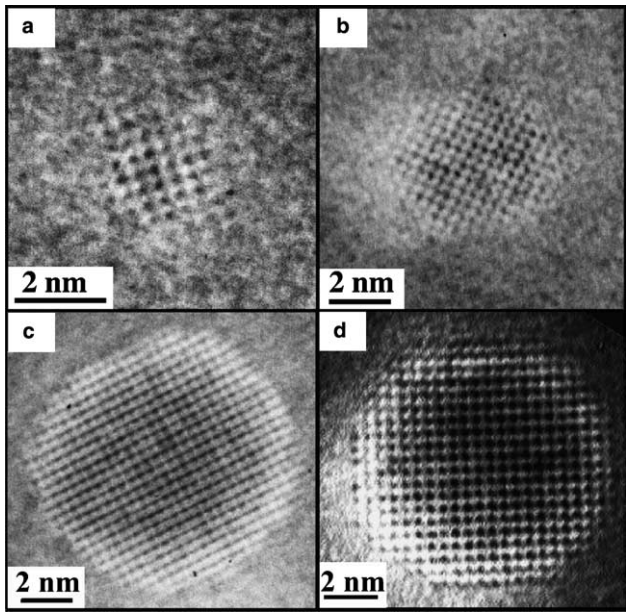

Fig. 3. High-resolution electron microscope images ([1 0 0] zone axis) of Al_3Sc precipitates in an Al–2.2 Mg–0.12 Sc at.% alloy after aging at 300 °C for: (a) 0.5 h; (b) 5 h; (c) 1040 h; and (d) Al_3Sc precipitate obtained in an Al–0.18 at.% Sc alloy after aging at 300 °C for 350 h [3].

When aging is performed at 350 °C for 24 h, the precipitate morphology is also approximately spheroidal (Fig. 4(a)). After aging at 400 °C for 2 h, the Al_3Sc precipitates exhibit irregular shapes as illustrated by the small protrusions on the precipitates in Fig. 4(b). Rod-

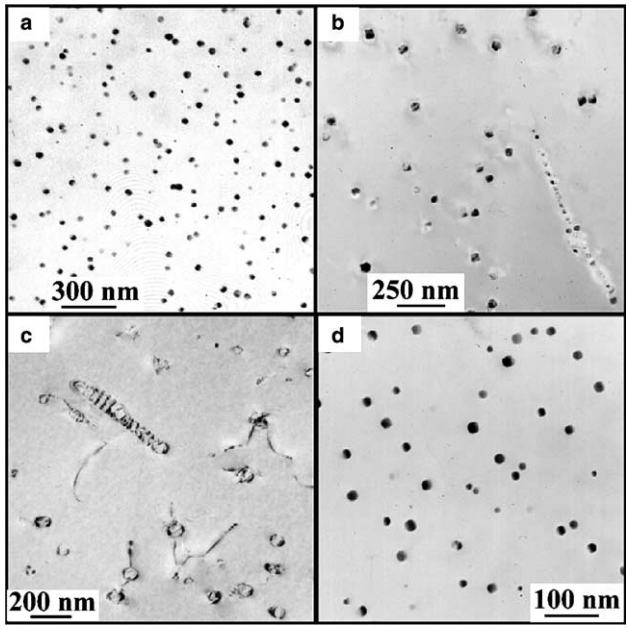

Fig. 4. CTEM micrographs of Al_3Sc precipitates after aging at: (a) 350 °C for 24 h; (b) 400 °C for 2 h; (c) 400 °C for 240 h; (d) 300 °C for 24 h followed by 400 °C for 24 h. The micrographs (a), (c), and (d) are dark-field images obtained using the 1 0 0 superlattice reflection.

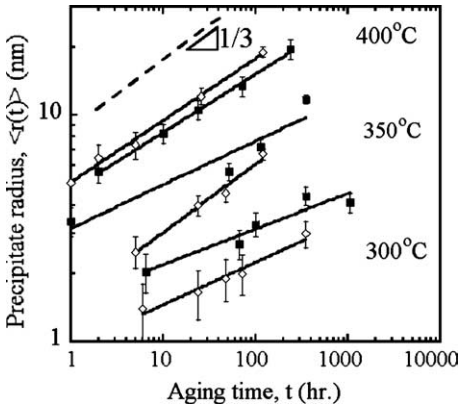

Fig. 5. Log–log plot of the average precipitate radius ($\langle R(t)\rangle$) as function of aging time at 300, 350 and 400 °C in the Al–2.2 Mg–0.12 Sc at.% (filled squares) and the Al–0.18 at.% Sc alloys [3] (open diamonds) versus aging time, yielding the value of the coarsening exponent, k_{KV}, in Eq. (2). The error bars correspond to one standard deviation.

like Al_3Sc precipitates, aligned along the [1 0 0] or [1 1 0] crystallographic directions, are also observed. These rods are semi-coherent with regularly spaced interfacial misfit dislocations, at an average dislocation spacing of 30 nm (Fig. 4(c)). For the present study, a pre-aging treatment at 300 °C for 24 h was performed, before aging at 400 °C, to produce high number densities of precipitates with more regular morphologies, which allows for the comparison and accurate measurement of precipitate dimensions. The resulting precipitate morphology appears cuboidal with facets parallel to the {1 0 0} planes (Fig. 4(d)). The α-Al/Al_3Sc interface remains coherent for precipitate radii to about 15 nm.

3.1.2. Precipitate dimensions

Average precipitate radii were obtained using both CTEM and HREM. During aging at 300 °C, the average precipitate radius, $\langle R(t)\rangle$, increases with aging time, from 1.1 nm after 0.5 h aging to 4.1 nm after 1040 h, as shown by representative HREM micrographs in Fig. 3. Fig. 5 displays the increasing average precipitate radius, $\langle R(t)\rangle$, with increasing aging time at 300, 350 or 400 °C. Note that in the case of cuboidal precipitates, the dimension corresponds to the average length along [1 0 0] directions.

3.2. Atom-probe tomography measurements

Measurements of Sc concentrations in the α-matrix were obtained from APT analyses of tips in the as-quenched state and after aging at 300 °C for 0.33 to 1040 h. The Mg concentration in the α-Al matrix is independent of aging time and is equal to 2.1 ± 0.4 at.%, which is very close to the nominal composition of the alloy, i.e., 2.2 at.%. The Sc concentration in the α-Al matrix decreases with increasing aging time from 0.166 ± 0.005 at.% after homogenization, to a value of 0.014 ± 0.001 at.% after 1040 h, as listed in Table 1. All error bars are equal to ±one standard deviation of the mean, unless stated otherwise.

4. Discussion

4.1. Precipitate morphologies

4.1.1. Morphology after aging at 300 °C

The equilibrium morphology of the Al_3Sc precipitates observed in the dilute Al–Sc system after aging at 300 °C for 250 h exhibits facets on the {1 0 0}, {1 1 0} and {1 1 1} planes and its geometry corresponds to a great rhombicuboctahedron [3]. The HREM micrographs of Al_3Sc precipitates obtained after aging the Al–Mg–Sc alloy at 300 °C for 1040 h, however, did not show the same faceted morphology. To illustrate the effect of Mg additions, the faceted morphology of an Al_3Sc precipitate obtained in an Al–0.18 at.% Sc alloy after aging at 300 °C for 350 h is displayed in Fig. 3(d). The equilibrium shape of a precipitate is determined by minimizing the sum of the interfacial and the elastic energies at constant volume. The relative contribution of each term is evaluated using the parameter [21]

$$L = \frac{C_{44}\varepsilon^2 l}{\gamma}, \tag{1}$$

Table 1
Average composition of the α-Al matrix as function of aging time at 300 °C

Time (s)	Total number of ions (10^6)	Al (at.%)	Mg (at.%)	Sc (at.%)
Nominal	–	97.68	2.2	0.12
As quenched	0.8	97.4 ± 0.02	2.41 ± 0.02	0.166 ± 0.005
1200	2.2	97.4 ± 0.01	2.46 ± 0.01	0.119 ± 0.002
1800	1.7	97.6 ± 0.01	2.29 ± 0.01	0.105 ± 0.003
7200	0.66	98.3 ± 0.02	1.66 ± 0.02	0.045 ± 0.003
18,000	1.4	97.7 ± 0.01	2.26 ± 0.01	0.044 ± 0.002
86,400	0.044	98.4 ± 0.06	1.56 ± 0.06	0.029 ± 0.008
3,60,000	0.55	98.3 ± 0.02	1.68 ± 0.02	0.016 ± 0.002
37,44,000	0.69	97.6 ± 0.02	2.35 ± 0.02	0.014 ± 0.001

where γ is an average value of the interfacial free energy, C_{44} is the shear modulus, ε is the lattice parameter misfit, and l is the characteristic size of the precipitates. It was shown, employing Eq. (1), that the shape of the Al_3Sc precipitates in the binary Al–Sc system is controlled by the interfacial free energy of the system [3,4]. The addition of Mg increases the lattice parameter of Al [22] and therefore decreases the lattice parameter mismatch to $\varepsilon = 0.0062$ at 300 °C; the elastic constants are essentially constant with Mg additions [23], and C_{44} is 28.5 GPa [24]; the interfacial free energy is also reduced by Mg segregation [4,18], and an experimental value, $\gamma = 140$ mJ m^{-2}, is calculated in Section 4.3. The ratio of the elastic energy to the interfacial free energy, L, is then equal to 0.06 for a precipitate diameter of 8 nm, and the morphology of the Al_3Sc precipitates in the presence of Mg is therefore also controlled by the interfacial free energy.

The change in morphology of the Al_3Sc precipitates with Mg addition from faceted to approximately spheroidal is associated with a change in the value of interfacial free energies. In particular, as suggested by a Wulff plot, the reduction of the {1 0 0} facet lengths corresponds to a smaller decrease of {1 0 0} energy relative to the interfacial free energies for the {1 1 0} and {1 1 1} facets, leading to a more rounded or approximately spheroidal morphology. The decrease of an average value of the interfacial free energy is demonstrated by segregation of Mg at the α-Al/Al_3Sc heterophase interface, as described in quantitative detail [4,18].

4.1.2. Morphology after aging at 400 °C

Growth instabilities have previously been observed in the dilute binary Al–Sc system, as the Sc supersaturation decreases [3,4,25], and the complex shapes observed in this Al–Mg–Sc alloy are comparable to the shapes that we observed in the binary Al–0.12 at.% Sc alloy aged at 350 °C [25]. The hypothesis of shape instability is confirmed by the more regular shapes obtained after an initial aging at 300 °C followed by a second aging treatment at 400 °C. The development of growth instabilities is most likely due to the lower number density of precipitates and concomitant decreased diffusion fields at early times, so that the precipitate morphology is controlled by growth conditions [26]. The development of rod-like Al_3Sc precipitates, about 300–500 nm in length, with irregular widths suggests formation by coagulation of existing precipitates, as suggested in [26,27]. Coherency loss may occur when the precipitate's dimension is large enough and the spacing between the misfit dislocations is of the order of a/ε, where $\varepsilon \approx 0.83\%$ is the lattice parameter misfit at 300 °C between the α-Al matrix containing 2.2 at.% Mg and the Al_3Sc phase [22,28], and $a \approx 0.2$ nm is the spacing between {2 0 0} planes. The calculated equilibrium dislocation spacing is therefore 32 nm, in good agreement with the experimental interfacial dislocation spacing observed for the rod-like precipitates (Fig. 4(b)).

4.2. Coarsening behavior

4.2.1. Assumptions of the coarsening model

The model developed by Kuehmann and Voorhees (KV) [1] to describe Ostwald ripening of second-phase spherical precipitates in a ternary system utilizes several assumptions that need to be discussed for the case of the Al_3Sc precipitates in the Al–Mg–Sc system. First, the coarsening behavior of the Al_3Sc phase is studied for precipitates with close to spheroidal morphologies, that is, precipitates obtained after aging at 300, 350, or 300 °C followed by 400 °C.

Second, it is assumed that no competing mechanisms contribute to the overall increase of the precipitates' dimensions. In particular, nucleation and growth of the precipitates are terminated and coarsening occurs by diffusional mass transfer from small precipitates with high interfacial curvatures to larger precipitates with lower interfacial curvatures. According to [29], the number density of Al_3Sc precipitates in a binary Al–0.12 at.% Sc alloy commences decreasing for an aging time longer than about 2.78 h at 288 °C and 0.56 h at 343 °C, which indicates that nucleation of new Al_3Sc precipitates is complete and the system has entered the coarsening regime. In considering the coarsening behavior, experimental data are therefore recorded for aging times longer than about 1 h.

The composition of the coarsening Al_3Sc phase is assumed to have reached its equilibrium bulk value, $c_e^{\beta}(\infty)$, as given by the phase diagram, Fig. 1. The measured compositions (APT) of all the Al_3Sc precipitates is indeed close to the stoichiometric composition, even at the shortest aging times, and the variations with aging times of the Sc concentration in the Al_3Sc phase, as reported by Sano et al. [30], employing one-dimensional atom-probe microscopy, are not confirmed. The composition of the Al_3Sc precipitates is also uniform within the precipitate volume [19]. No Al_3Sc precipitates with non-stoichiometric composition were ever observed. The time independent composition of the Al_3Sc precipitates is consistent with one of the assumptions of the LSW model of coarsening for a binary alloy.

Because the predicted coarsening rate constants for the binary Al–Sc [3] and ternary Al–Mg–Sc (Table 3) alloys are comparable, the off-diagonal terms of the diffusion tensor are neglected, which implies that diffusional interactions between Sc and Mg are neglected: this is a strong assumption as it neglects the flux of atoms carried by the off-diagonal terms. Furthermore, the chemical potential of a vacancy is taken equal to zero.

In the KV mathematical treatment of coarsening, the system is considered to be in a quasi-steady-state, that is,

$t \to \infty$, and in this asymptotic time limit, the time dependencies of the mean precipitate radius, $\langle R(t)\rangle$, and the Sc concentration in the matrix, $C_e^{\alpha}(t)$, are given by [11,12,31]

$$\langle R(t)\rangle^n - \langle R(t_o)\rangle^n = k_{KV}(t - t_o), \quad (2)$$

$$c_{Sc}^{\alpha}(t) - c_{Sc}^{\alpha}(\infty) = \kappa_{KV} t^m, \quad (3)$$

where $n = 3$ and $m = -1/3$ are the predicted exponents; $c_{Sc}^{\alpha}(\infty)$ is the solid-solubility of Sc in the α-Al phase at the aging temperature; and k_{KV} and κ_{KV} are two different rate constants, which are dependent on the detailed thermodynamics of the system, the average interfacial free energy, and the diffusion coefficients of Mg and Sc in Al. Eqs. (2) and (3) exhibit the same time dependencies for both binary and ternary systems, albeit with quite different kinetic rate constants. The agreement between the experimental data and the model predictions is discussed in the following subsections.

4.2.2. Temporal evolution of the precipitate radius

The form of Eq. (2) implies two variables, n and $\langle R(t_o)\rangle$. In the following treatment, $\langle R(t_o)\rangle^3$ is neglected [15], and Eq. (2) becomes $\langle R(t)\rangle^n \cong k_{KV}t$, which implies that a log–log plot of the average precipitate radius, $\langle R\rangle$, versus aging time yields a slope of $1/n$. Figs. 5 and 6 indicates that the experimental slopes are smaller than the value 1/3, and increase with increasing temperature. The ternary system also appear to have smaller coarsening exponents than the binary Al–0.18 at.% Sc alloy, used as a reference [3], at 300 and 350 °C (Table 2). Several authors have also reported lower values of the coarsening exponents, in particular for the coarsening behavior of Ni–Al alloys [32], where Ti additions affect the coarsening rate, and for the behavior of dilute Al–Sc alloys with addition of Zr [33]. Slopes smaller than 1/3, as determined from Fig. 5, could be an indication that the system is in a transient coarsening regime or that the exact atomistic diffusion mechanisms (that is, the off-diagonal terms in the diffusion tensor and the chemical potential of a vacancy may be significant) by which coarsening takes place need to be taken into account to explain the coarsening kinetics in detail. In particular, lattice kinetic Monte Carlo simulations with a vacancy diffusion mechanism accounting for possible asymmetries in the vacancy mobility and concentrations between precipitate and matrix phases predict smaller time exponents [34]. A possible explanation for the fact that the slopes are closer to 1/3 at 350 and 400 °C than at 300 °C is that the assumption of a quasi-steady-state is not achieved for the lower temperatures due to slower diffusion, but is obtained when aging at 350 and 400 °C: at 300 °C, $n = 0.16 \pm 0.02$; at 350 °C it is 0.19 ± 0.03; and at 400 °C it is 0.26 ± 0.06, which are all less than 1/3. In the following analysis, the ternary Al–Mg–Sc alloy is, however, assumed to obey the assumption of quasi-steady-state coarsening described in [1] for all aging temperatures.

Table 2
Coarsening exponents measured from the plots displayed in Fig. 5 for the Al–0.18 at.% Sc and Al–2.2 at.% Mg–0.12 at.% Sc alloys at three different aging temperatures

	300 °C	350 °C	400 °C
Al–0.18 at.% Sc	0.18 ± 0.01	0.3 ± 0.02	0.27 ± 0.01
Al–2.2 at.% Mg–0.12 at.% Sc	0.16 ± 0.02	0.19 ± 0.03	0.26 ± 0.06

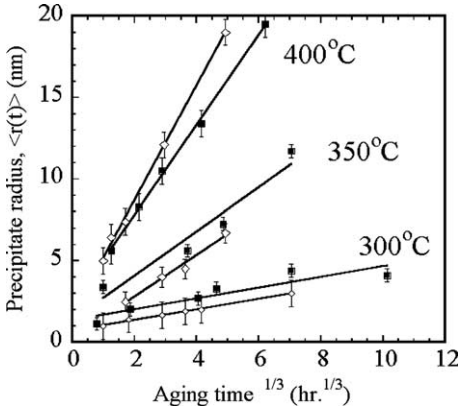

Fig. 6. Mean precipitate radius ($\langle R(t)\rangle$) versus (aging time)$^{1/3}$ ($t^{1/3}$) at 300, 350 or 400 °C (the latter samples were pre-aged at 300 °C for 24 h prior to aging at 400 °C), comparing the coarsening behavior of an Al–0.12 at.% Sc alloy (open diamonds) with an Al–2.2 at.% Mg–0.12 at.% Sc alloy (filled squares). The error bars correspond to one standard deviation.

The coarsening kinetics increase as the aging temperature increases, as shown by the increasing slopes of the fitted curves in Fig. 6. The average precipitate radius is larger for the Al–2.2 Mg–0.12 Sc at.% alloy at 300 and 350 °C than for the binary Al–0.18 at.% Sc alloy. The inverse trend at 400 °C may arise from the different initial conditions; the binary alloy was directly aged at 400 °C, whereas the ternary alloy underwent a pre-aging treatment at 300 °C. The smaller Sc supersaturation (~0.12 at.% Sc) than in the binary alloy (~0.18 at.% Sc) is associated with a smaller thermodynamic driving force (Fig. 1) and leads to a smaller number density of Al_3Sc precipitates and larger precipitates, which is consistent with nucleation theory.

Table 3 presents the measured values of the kinetic rate constants and a comparison with the coarsening kinetics of the binary Al–0.18 at.% Sc [3] and the ternary Al–2.2 Mg 0.12 Sc at.% alloys. By comparing the experimental kinetic constants, k, with the asymptotic solutions of the LSW and KV models (Table 3), better agreement is found for the binary Al–Sc alloy (LSW) than for the ternary Al–Sc–Mg (KV).

4.2.3. Temporal evolution of the Sc matrix concentration

As the Al_3Sc precipitates coarsen, the Sc concentration in the matrix systematically decreases, as observed

Table 3
Solid-solubility of Sc in primary α-phase ($c^{\alpha}_{Sc}(\infty)$) and in the Al_3Sc phase ($c^{\beta}_{Sc}(\infty)$); solid-solubility of Mg in primary α-phase and in the Al_3Sc phase; diffusion coefficient of Mg and Sc in Al; measured and calculated coarsening constants (k_{KV} and κ_{KV}) for the Al–2.2 at.% Mg–0.12 at.% Sc alloy for three different temperatures; and measured and calculated solid-solubility constants (κ_{KV}) at 300 °C

	300 °C	350 °C	400 °C
Measured solid-solubility of Sc in Al–2.2at.% Mg (this work)	$8.9 \pm 3 \times 10^{-5}$	–	–
Calculated solid-solubility of Sc in Al[a]	7.20×10^{-6}	2.28×10^{-5}	6.00×10^{-5}
Measured solid-solubility of Sc in Al_3Sc[b]	0.274 ± 0.016	–	–
Calculated solid-solubility of Sc in Al_3Sc[a]	0.25	0.25	0.25
Calculated solid-solubility of Mg in Al_3Sc[a]	0	–	–
Diffusion coefficient of Sc in Al ($m^2\ s^{-1}$)[c]	8.84×10^{-20}	1.63×10^{-18}	1.95×10^{-17}
Diffusion coefficient of Mg in Al ($m^2\ s^{-1}$)[d]	1.62×10^{-16}	1.46×10^{-15}	9.44×10^{-15}
Measured k_{KV} ($m^3\ s^{-1}$) (this work)	$1.6 \pm 0.7 \times 10^{-32}$	$1.3 \pm 0.1 \times 10^{-30}$	$8.3 \pm 0.2 \times 10^{-30}$
Calculated k_{KV} ($m^3\ s^{-1}$)	3.4×10^{-33}	2.0×10^{-31}	5.9×10^{-30}
Measured ternary k/calculated ternary k	4.7	6.5	1.4
Measured k ($m^3\ s^{-1}$) in the binary Al–0.3 wt.% Sc alloy[e]	$2.0 \pm 0.4 \times 10^{-32}$	$6.9 \pm 1.1 \times 10^{-31}$	$1.6 \pm 0.12 \times 10^{-29}$
Measured ternary k/measured binary k	0.8	1.9	0.5
Measured κ_{KV} (at.fr. $s^{1/3}$) (this work)	$8.8 \pm 1 \times 10^{-3}$	–	–
Calculated κ_{KV}(at.fr. $s^{1/3}$)	1.4×10^{-3}	–	–

[a] Ref. [8].
[b] Ref. [18].
[c] Ref. [5].
[d] Ref. [36].
[e] Ref. [3].

by APT (Table 1). The Sc concentration in the α-Al matrix first exhibits a steep decrease between 0.33 and 0.5 h, Fig. 7, corresponding to nucleation and growth of Al_3Sc precipitates. After 0.5 h, the Sc concentration slowly decreases. The data are plotted in Fig. 7 according to Eq. (3). To check the agreement between the experimental data and the KV model, m is first taken equal to −1/3 to calculate a value of the equilibrium Sc concentration in α-Al, $c^{\alpha}_{Sc}(\infty)$, which is the intercept of the fitted line and the solid-solubility axis in Fig. 7, corresponding to $t = \infty$. The extrapolated value of the solid solubility is $(8.9 \pm 3) \times 10^{-3}$ at.% Sc. Prior data obtained by Sano et al. [30] on an Al–0.25 wt.% Sc alloy aged at 300 °C, using a one-dimensional atom-probe microscope, lead to a higher value, that is, 1.5×10^{-2} at.% Sc. Both our measurement and Sano et al.'s of the Sc solid-solubility are higher, however, than the value calculated from thermodynamic or resistivity data; that is, the Sc solid-solubility in Al–2.2 at.% Mg at 300 °C is 7.2×10^{-4} at.% assuming no solubility of Mg in Al_3Sc and 4.8×10^{-4} at.% if the Mg solubility in the Al_3Sc phase is finite according to Murray [8]. In binary Al–Sc alloys, the solid-solubility at 300 °C is 1.7×10^{-3} at.% Sc according to Fujikawa's resistivity measurements [35]. The advantage of APT over resistivity measurements is the direct determination of concentration values, which

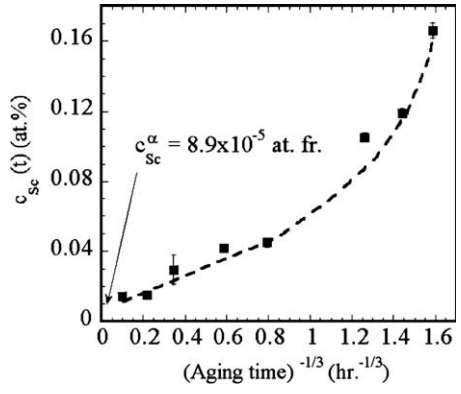

Fig. 7. Scandium concentration in the α-matrix ($c^{\alpha}_{Sc}(t)$) as function of (aging time)$^{-1/3}$ at 300 °C, yielding equilibrium solid-solubility of Sc in this Al–Mg–Sc alloy, $c^{\alpha}_{Sc}(\infty) = 8.9 \times 10^{-5}$ at.fr. The error bars correspond to one standard deviation.

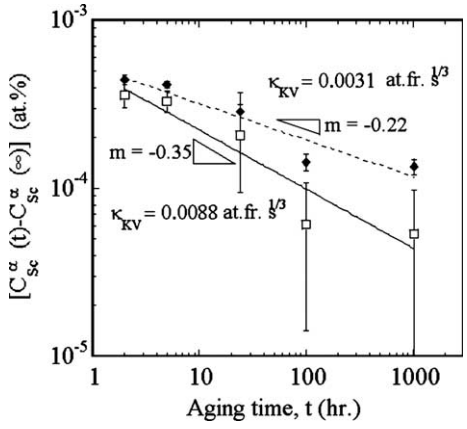

Fig. 8. Log–log plot of the scandium supersaturation in the α-matrix, $[(c^{\alpha}_{Sc}(t)) - c^{\alpha}_{Sc}(\infty)]$, versus aging time ($t$). The empty squares are obtained using our experimental value of the Sc solubility in Al at 300 °C; the filled diamonds are obtained using the Sc solid-solubility data from [7]. The error bars correspond to one standard deviation.

do not require calibration standards. Fig. 8 displays a log–log plot of $[c^{\alpha}_{Sc}(t) - c^{\alpha}_{Sc}(\infty)]$ (the Sc supersaturation) versus aging time, and the slope of the fitted straight line, -0.35 ± 0.05, is close to the theoretical value of $-1/3$, predicted by the KV coarsening model for a ternary alloy. The measured value of the coarsening constant is then $\kappa_{KV} = (8.8 \pm 1) \times 10^{-3}$ at.fr. $s^{1/3}$, which is a factor of six greater than the calculated constant, 1.4×10^{-3}at.fr. $s^{1/3}$ (see Eq. (9)).

4.3. Interfacial free energy and diffusion coefficient

The coarsening rate constant, k_{KV}, for the temporal evolution of the precipitate radius in a ternary alloy is given by [1]

$$k_{KV} = \frac{8\gamma V_m}{9\Lambda}, \tag{4}$$

where $V_m = 1.035 \times 10^{-5}$ m^3 mol^{-1} is the average atomic volume per mol of the Al_3Sc phase, deduced from $V_m = N_a a^3/4$ (N_a is Avogadro's number, $a = 0.4196$ nm is the lattice parameter of Al_3Sc [28]), γ is an average interfacial free energy at 300 °C. The coefficient Λ is given by

$$\Lambda = \frac{\Delta c_{Sc}}{D_{Sc}}\left(\Delta c_{Sc} G''_{ScSc} + \Delta c_{Mg} G''_{ScMg}\right) + \frac{\Delta c_{Mg}}{D_{Mg}}\left(\Delta c_{Sc} G''_{ScMg} + \Delta c_{Mg} G''_{MgMg}\right), \tag{5}$$

where $\Delta c_i = c^{\beta}_i(R) - c^{\alpha}_i(R) \approx c^{\beta}_i(\infty) - c^{\alpha}_i(\infty)$; $c^{\alpha/\beta}_i(R)$ are the concentrations in the α- and β-phases (matrix and precipitate phases) near the precipitate interface; the $c^{\alpha/\beta}_i(\infty)$ are the concentrations far from the α-Al/Al_3Sc interfaces in the α-Al matrix. This approximation implies that a possible enhancement of solute concentration at the curved precipitate interface is negligible in the evaluation of the Δc_i. The Sc concentration in the α-Al matrix, at any aging time, is negligible compared to the Sc concentration in the Al_3Sc precipitates, $c^{\beta}_{Sc} = 27.4 \pm 1.5$ at.% Sc, which is invariant with time, within the experimental error, from the earliest time (0.33 h) to the longest coarsening time (1040 h) as measured by APT [18], and $\Delta c_{Sc} = c^{\beta}_{Sc} - c^{Al\text{–}2.2\ Mg}_{Sc} \approx c^{\beta}_{Sc}$. The Mg concentration in the α-Al matrix is also approximately a constant; the Mg concentration in the precipitates is, however, evolving as shown in [18], but for the sake of simplicity it is taken equal to be zero, $c^{\beta}_{Mg} = 0$ at.%. The G''_{ij} are the second derivatives of the Gibbs free energy with respect to the concentrations of i and j, with i, j = Sc, Mg; the D_is are the diffusion coefficients of Sc and Mg in Al–2.2 at.% Mg. Assuming the α-Al phase is described by dilute ideal solid-solution theory, the derivatives of the Gibbs free energy are given by

$$G''_{ScSc} = \frac{RT\left(1 - c^{\alpha}_{Mg}(\infty)\right)}{\left[c^{\alpha}_{Sc}(\infty)\left(1 - c^{\alpha}_{Sc}(\infty) - c^{\alpha}_{Mg}(\infty)\right)\right]}, \tag{6}$$

$$G''_{ScMg} = \frac{RT}{\left[1 - c^{\alpha}_{Sc}(\infty) - c^{\alpha}_{Mg}(\infty)\right]} \quad \text{and} \tag{7}$$

$$G''_{MgMg} = \frac{RT\left(1 - c^{\alpha}_{Sc}(\infty)\right)}{\left[c^{\alpha}_{Mg}(\infty)\left(1 - c^{\alpha}_{Sc}(\infty) - c^{\alpha}_{Mg}(\infty)\right)\right]}. \tag{8}$$

The kinetic rate constant κ_{KV} describing the Sc concentration in the matrix is given by [1]

$$\kappa_{KV} = \frac{(3\gamma V_m)^{2/3}\Lambda^{1/3}\Delta c_{Sc}}{\left[\Delta c_{Sc}\left(\Delta c_{Sc} G''_{ScSc} + \Delta c_{Mg} G''_{ScMg}\right) + \Delta c_{Mg}\left(\Delta c_{Mg} G''_{MgMg} + \Delta c_{Sc} G''_{ScMg}\right)\right]}. \tag{9}$$

From measurements of both precipitate mean radius, $\langle R(t)\rangle$, and the temporal evolution of the matrix solute concentration, $c^{\alpha}_{Sc}(t)$, it is possible to calculate an average value of the interfacial free energy and a value of the diffusion coefficient at 300 °C, independently of one another, as first shown by Ardell for a binary alloy [37]. Using Eqs. (4)–(9), the relationship for the interfacial free energy is given by

$$\gamma = \frac{\kappa_{KV} k_{KV}^{1/3}\left[\Delta c_{Sc}\left(\Delta c_{Sc} G''_{ScSc} + \Delta c_{Mg} G''_{ScMg}\right) + \Delta c^{\alpha}_{Mg}\left(\Delta c_{Sc} G''_{ScMg} + \Delta c_{Mg} G''_{MgMg}\right)\right]}{[2V_m \Delta c_{Sc}]} \tag{10}$$

and the diffusion coefficient D_{Sc} in the ternary alloy is obtained from

$$\frac{4}{9}\frac{\kappa_{KV}}{\Delta c_{Sc}}\frac{\Delta c_{Sc}\left(\Delta c_{Sc} G''_{ScSc} + \Delta c_{Mg} G''_{ScMg}\right) + \Delta c^{\alpha}_{Mg}\left(\Delta c_{Sc} G''_{ScMg} + \Delta c_{Mg} G''_{MgMg}\right)}{k_{KV}^{2/3}\Delta c_{Sc}} = \frac{\Delta c_{Sc}}{D_{Sc}}\left(\Delta c_{Sc} G''_{ScSc} + \Delta c_{Mg} G''_{ScMg}\right) + \frac{\Delta c_{Mg}}{D_{Mg}}\left(\Delta c_{Sc} G''_{ScMg} + \Delta c_{Mg} G''_{MgMg}\right). \tag{11}$$

Since $\Delta c_{Sc} \cong 0.25 \gg \Delta c_{Mg} \cong 0.022$, and $D_{Sc} \ll D_{Mg}$ at 300 °C (Table 1), Eq. (11) simplifies to

$$D_{Sc} = \frac{9\Delta c_{Sc}^2\left(\Delta c_{Sc} G''_{ScSc} + \Delta c_{Mg} G''_{ScMg}\right)k_{KV}^{2/3}}{4\kappa_{KV}\left(\Delta c_{Sc} G''_{ScSc} + \Delta c_{Mg} G''_{ScMg}\right) + \Delta c_{Mg}\left(\Delta c_{Sc} G''_{ScMg} + \Delta c_{Mg} G''_{MgMg}\right)}. \tag{12}$$

The experimental values of the equilibrium Sc solid-solubility, $c^{\alpha}_{Sc}(\infty) = 8.9 \times 10^{-5}$ at.fr., the kinetic constant for the time dependence of the Sc concentration in the matrix, $\kappa_{KV} = 8.8 \times 10^{-3}$ at.fr. $s^{1/3}$ (Fig. 8), and the coarsening constant for the time dependence of the precipitate radius, $k_{KV} = 1.69 \times 10^{-32}$ m^3 s^{-1} (Table 3), yield a diffusion coefficient of $(1.2 \pm 0.6) \times 10^{-20}$ m^2 s^{-1} and an interfacial free energy of 158 ± 36 mJ m^{-2} at 300 °C. Assuming a lower Sc solid-solubility value, such as the values given by the thermodynamic assessments, 7.2×10^{-6} at.fr. [8], the interfacial free energy becomes extremely high, 1.95 J m^{-2}, which lends credence to our higher experimental value of the Sc solubility at

300 °C, as compared to the value calculated from assessments of the thermodynamic data. Our calculated value of the Sc diffusion coefficient at 300 °C is reasonable, since the diffusion coefficient for Sc in pure Al at 300 °C is 8.84×10^{-20} m^2 s^{-1} [5], which differs only by a factor of six for the diffusivity of Sc in this Al–Mg–Sc alloy.

The value of the interfacial energy, 158 ± 36 mJ m^{-2}, is comparable to the experimental values previously reported for the α-Al/Al_3Sc heterophase interface without Mg addition: 78–125 mJ m^{-2} (Hyland [38]), 41–63 mJ m^{-2} (Jo and Fujikawa [35]), 105 mJ m^{-2} (Novotny and Ardell [25]), 120 mJ m^{-2} (Iwamura and Miura [39]), 20–300 mJ m^{-2} (Royset and Ryum [40]), 218 mJ m^{-2} (Watanabe et al. [41]), and 57 mJ m^{-2} increasing with precipitate radius (Robson et al. [42]). Note, however, the wide range of values. It is also comparable to the value obtained from first-principles calculations for the α-Al/Al_3Sc without Mg, 175 mJ m^{-2} [2]. Taking into account the Mg segregation at the α-Al/Al_3Sc interface [18], a decrease in the interfacial free energy in the ternary Al–Mg–Sc system is anticipated and is estimated to be ~15 mJ m^{-2} [4].

The smaller calculated values of the diffusion coefficient of Sc in Al and of the interfacial free energy as compared to the binary Al–Sc system should lead to slower coarsening kinetics according to Eq. (3). The experimental data do not, however, exhibit any significant differences between the binary and ternary data. There are, however, significant differences in the exponents n for $\langle R(t)\rangle$, see Table 2, for the two alloys; the measured ternary rate constants divided by the measured binary k all differ from unity. Neither the binary Al–Sc nor the ternary Al–Mg–Sc alloy exactly fit the LSW or KV coarsening models, respectively, and the ratios of the measured to the calculated ternary rate constants are all significantly greater than unity. The values are 4.7 at 300 °C, 6.5 at 350 °C, and 1.4 at 400 °C (Table 3), which reinforces the point that the rate constant, k, is temperature dependent.

The calculated coarsening constants obtained using Eqs. (5)–(9) and the values of γ and D_{Sc} are presented in Table 3, and they show qualitative agreement with the measured values. The calculated value of κ_{KV} at 300 °C is 1.4×10^{-3} at.fr. s$^{1/3}$, and the measured value is 8.8×10^{-3} at.fr s$^{1/3}$, which implies a factor of 6.3 greater than the calculated value. Firstly, this may be because the second derivative of the free energy is most likely overestimated by employing an ideal solid-solution model. Secondly, it may be due to the neglect of the off-diagonal terms in the diffusion tensor or the assumption of zero for the vacancy chemical potential. Eq. (3) therefore implies that the value of the interfacial free energy derived above is also an upper bound, whereas the value of the diffusion coefficient of Sc in Al at 300 °C obtained from Eq. (12) is a lower bound.

5. Conclusions

The study of coarsening kinetics in the ternary Al–2.2 Mg–0.12 Sc at.% alloy between 300 and 400 °C are qualitatively similar to those of the binary Al–0.18 at.% Sc alloy [3], but there are quantitative differences:

- The morphology of the Al_3Sc ($L1_2$) precipitates, as observed by HREM, after aging at 300 °C is approximately spheroidal and the faceted morphologies of the Al_3Sc precipitates, which results in great rhombicuboctahedra, in an Al–0.18 at.% Sc binary alloy are not observed (Fig. 3). This implies that the {1 1 0} and {1 1 1} interfacial free energies are most likely decreasing to values close to the one for {1 0 0} α-Al/Al_3Sc to yield an approximately isotropic interfacial free energy, thereby producing an approximately spheroidal precipitate morphology.
- Irregular Al_3Sc precipitate shapes, attributed to unstable growth, are observed after aging directly at 400 °C (Fig. 4); however, by pre-aging at 300 °C, regular Al_3Sc precipitate morphologies are obtained.
- The coarsening kinetics of the Al_3Sc precipitates in an Al–2.2 Mg–0.12 Sc at.% alloy are analyzed using a detailed coarsening model developed by Kuehmann and Voorhees [1] for dilute ternary alloys. The KV model is based on the Umantsev–Olson [17] analytical treatment of coarsening in multicomponent alloys.
- The exponent describing the time dependence of the average precipitate radius, $\langle R\rangle$, is never equal exactly to 1/3 for the three aging temperatures considered in this study and is temperature dependent; that is, it increases with increasing aging temperature.
- The ratios of the measured to the calculated ternary rate constants are different from unity and vary from 1.4 to 6.5 for aging temperatures varying from 300 to 400 °C; this may be due to the neglect of the off-diagonal terms in the diffusion tensor and/or taking the vacancy chemical potential equal to zero.
- In the coarsening stage, the Sc concentration in the matrix was measured by APT and approximate agreement was found with the t^{-n} dependence, with $n = 0.35 \pm 0.06$ for the supersaturation of Sc, as predicted by the KV model (Fig. 8).
- Independent measurements of the α-Al/Al_3Sc interfacial free energy and the diffusion coefficient of Sc in Al–Sc–Mg are determined based on the coarsening kinetics of the average precipitate radius (HREM) and Sc concentration (APT), and good agreement is found between the measured values of the interfacial free energy at 300 °C, 158 ± 36 mJ m^{-2}, and predictions based on first-principles calculations [2], 160 mJ m^{-2}, and between the diffusion coefficient for Sc diffusion in Al–2.2 at.% Mg at 300 °C, $(1.4 \pm 0.6) \times 10^{-20}$ m^2 s^{-1}, and existing values for the diffu-

sivity of Sc in pure Al [5], $(8.84) \times 10^{-20}$ $m^2 s^{-1}$. The unique aspect of this approach lies in the direct measurement of the Sc supersaturation in the α-Al matrix by APT. More details concerning the chemical aspects of the temporal evolution of Al_3Sc precipitates in this ternary Al–Mg–Sc alloy are given in [4,18].

Acknowledgments

This research is supported by the United States Department of Energy, Basic Sciences Division, under contract DE-FG02-98ER45721. The authors acknowledge Professors Mark D. Asta, David C. Dunand, and Peter W. Voorhees (Northwestern University) and Alexander Umantsev for interesting discussions, Dr. Joanne L. Murray (Alcoa) for kindly providing data on the Al–Mg–Sc phase diagram (Fig. 1), Dr. Roseanne Csencsits, formerly of Argonne National Laboratory, for use of the JEOL 4000EXII microscope at Argonne National Laboratory, and Alcoa Inc. and Ashurst Inc. for kindly supplying Al–Sc master alloys.

References

[1] Kuehmann CJ, Voorhees PW. Metall Mater Trans A 1996;27:937.
[2] Asta M, Ozolins V, Woodward C. JOM 2001;53:16.
[3] Marquis EA, Seidman DN. Acta Mater 2001;49:1909.
[4] Marquis EA. Ph.D. Thesis. Materials Science and Engineering Department, Northwestern University, 2002.
[5] Fujikawa SI. Defect Diffusion Forum 1997;143–147:115.
[6] Toporova LS, Eskin DG, Kharakterova ML, Dobatkina TB. Advanced aluminum alloys containing scandium. Amsterdam: Gordon & Breach; 1998.
[7] Royset J, Ryum N. Int Mater Rev 2005;50:1.
[8] Murray JL. [Personal communication].
[9] Pisch A, Grobner J, Schmidt-Fetzer R. Mater Sci Eng A 2000;289:123.
[10] Grobner J, Schmid-Fetzer R, Pisch A, Cacciamani G, Riani P, Parodi N, et al. Z Metallkd 1999;90:11.
[11] Wagner C. Z Elektrochem 1961;65:581.
[12] Lifshitz IM, Slyozov VV. Phys Chem Solids 1961;19:35.
[13] Sawtell RR, Jensen CL. Metall Trans A 1990;21:421.
[14] Chellman DJ, Ardell AJ. Acta Metall 1974;22:577.
[15] Fahrmann M, Fahrmann E, Pollock TM, Johnson WC. Metall Mater Trans A 1997;28:1943.
[16] Sequeira D, Calderon HA, Kostorz G, Pedersen JS. Acta Metall Mater 1995;43:3427;
Sequeira D, Calderon HA, Kostorz G, Pedersen JS. Acta Metall Mater 1995;43:3441.
[17] Umantsev A, Olson GB. Scripta Metall Mater 1993;29:1135.
[18] Marquis EA, Seidman DN, Asta M, Woodward C, Ozolins V. Phys Rev Lett 2003;91:036101.
[19] Marquis EA, Seidman DN, Dunand DC. Acta Mater 2003;51:4751.
[20] Seidman DN, Marquis EA, Dunand DC. Acta Mater 2002;50:4021;
Seidman DN, Marquis EA, Dunand DC. Acta Mater 2003;51:285.
[21] Thompson ME, Su CS, Voorhees PW. Acta Mater 1994;42:2107.
[22] Hatch JE. Aluminum: properties and physical metallurgy. Metals Park (OH): ASM; 1984.
[23] Metals Handbook. Materials Park (OH): ASM; 1990.
[24] Frost HJ, Ashby MF. Deformation mechanism maps. Oxford: Pergamon Press; 1982.
[25] Novotny GM, Ardell AJ. Mater Sci Eng A 2001;318:144.
[26] Ryum N. Acta Metall 1969;17:269.
[27] Izumi O, Oelschlagel D. Scripta Metall 1969;3:619.
[28] JCPDS – International Centre for Diffraction Data. v. 2.00, 1998.
[29] Hyland RW. Metall Trans A 1992;23:1947.
[30] Sano N, Hasegawa Y, Hono K. J Phys (Paris) 1987;48:C-337.
[31] Ratke L, Voorhees PW. Growth and coarsening: Ostwald ripening in material processing. Berlin, New York: Springer; 2001.
[32] Njah N, Dimitrov O. Acta Metall 1989;37:2559.
[33] Fuller CB, Seidman DN. Acta Mater [submitted].
[34] Roussel JM, Bellon P. Phys Rev B 2001;63:184114.
[35] Jo HH, Fujikawa SI. Mater Sci Eng A 1993;171:151.
[36] Rothman SJ, Peterson NL, Nowicki LJ, Robinson LC. Phys Status Solidi B 1974;63:K29.
[37] Ardell AJ. Interface Sci 1995;3:119.
[38] Hyland Jr RW, Stiffler RC. Scripta Mater 1991;24:473.
[39] Iwamura S, Miura Y. Acta Mater 2004;53:591.
[40] Royset J, Ryum N. Mater Sci Eng A 2005;396:409.
[41] Watanabe C, Kondo T, Monzen R. Metall Trans A 2004;35:3003.
[42] Robson JD, Jones MJ, Prangnell PB. Acta Mater 2005.